

Nitrogen Activation in a Mars–van Krevelen Mechanism for Ammonia Synthesis on $\text{Co}_3\text{Mo}_3\text{N}$

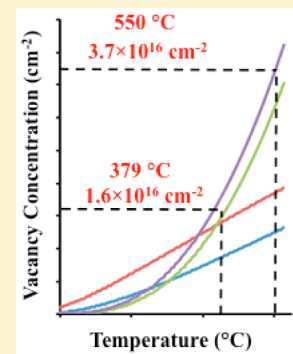
Constantinos D. Zeinalipour-Yazdi,^{*,†} Justin S. J. Hargreaves,[‡] and C. Richard A. Catlow^{*,†}

[†]Kathleen Lonsdale Materials Chemistry, Department of Chemistry, University College London, London, WC1E 6BT, U.K.

[‡]WestCHEM, School of Chemistry, University of Glasgow, Glasgow, G12 8QQ, U.K.

Supporting Information

ABSTRACT: $\text{Co}_3\text{Mo}_3\text{N}$ is one of the most active catalysts for ammonia synthesis; however, little is known about the atomistic details of N_2 adsorption and activation. Here we examine whether N_2 can adsorb and activate at nitrogen surface vacancies. We have identified the most favorable sites for surface nitrogen vacancy formation and have calculated vacancy formation free energies (and concentrations) taking into account vacancy configurational entropy and the entropy of N_2 at temperature and pressure conditions relevant to ammonia synthesis (380 – 550 °C, 100 atm) via a semiempirical approach. We show that 3-fold hollow bound nitrogen-containing (111)-surfaces have surprisingly high concentrations (1.6×10^{16} to $3.7 \times 10^{16} \text{ cm}^{-2}$) of nitrogen vacancies in the temperature range for ammonia synthesis. It is shown that these vacancy sites can adsorb and activate N_2 demonstrating the potential of a Mars–van Krevelen type mechanism on $\text{Co}_3\text{Mo}_3\text{N}$. The catalytically active surface is one where 3f-hollow-nitrogens are bound to the molybdenum framework with a hexagonal array of embedded Co_8 cobalt nanoclusters. We find that the vacancy-formation energy (VFE) combined with the adsorption energy can be used as a descriptor in the screening of materials that activate doubly and triply bonded molecules that are bound end-on at surface vacancies.



1. INTRODUCTION

According to IFA statistics there is a correlation between the global food production and the consumption of fertilizers.¹ Ammonia (NH_3) is the main ingredient of fertilizers industrially produced by the classical Haber-Bosch process which is considered one of the milestones in catalysis.² In this process, high-purity N_2 and H_2 are combined over a promoted Fe-based catalyst operating at high temperatures (350 – 500 °C) and pressures (150 – 350 atm).³ The process is energy intensive (28 – $166 \text{ GJ}\cdot\text{ton}^{-1} \text{ NH}_3$),⁴ and the production of H_2 requires the consumption mainly of natural gas and coal with the catalysts operating at elevated temperatures and pressure, which leads to the generation of various greenhouse gases. The very large worldwide production of ammonia, estimated to be more than 162 million metric tons annually,⁴ suggests that any improvement to the process or the catalyst potentially could have a major environmental and economic impact.

Cobalt molybdenum nitride ($\text{Co}_3\text{Mo}_3\text{N}$), which possesses the structure illustrated in Figure 1a–1b, and related tertiary nitrides ($\text{M}_x\text{M}'_y\text{N}$, where M a group VIB and M' a group VIII metal) with synthesis patented by researchers from Haldor Topsøe A/S⁵ are known to be active for ammonia synthesis at 400 °C and elevated pressures using a 3:1, $\text{H}_2:\text{N}_2$ mixture.^{6,7} $\text{Co}_3\text{Mo}_3\text{N}$ when doped with cesium ions (Cs^+) is one of the most active catalysts for ammonia synthesis, with higher turnover frequencies (TOF), larger than graphite-supported Ru and $\text{Fe}-\text{K}_2\text{O}-\text{Al}_2\text{O}_3$, both currently used industrially for ammonia synthesis. Kojima and Aika showed that Cs-promoted $\text{Co}_3\text{Mo}_3\text{N}$ had a 3-times higher rate for ammonia synthesis ($986 \mu\text{mol/h}\cdot\text{g}$) than the commercial $\text{Fe}-\text{K}_2\text{O}-\text{Al}_2\text{O}_3$ ($330 \mu\text{mol/h}\cdot\text{g}$) at 673 K under 0.1 MPa.⁶ The TOF for the production of 3.5% ammonia concentration at 400 °C and 50 bar was determined to be 19 , 14 , and 5 s^{-1} for $\text{Co}_3\text{Mo}_3\text{N}$, Ru, and Fe, respectively,⁸ indicating the potential application of Cs-promoted $\text{Co}_3\text{Mo}_3\text{N}$ for ammonia synthesis. Among the other ternary nitrides, $\text{Fe}_3\text{Mo}_3\text{N}$ has exhibited considerably better activity than the binary molybdenum nitrides (e.g., $\gamma\text{-Mo}_2\text{N}$, $\delta\text{-MoN}$),⁹ but it is still less active than $\text{Co}_3\text{Mo}_3\text{N}$. The importance of nitrogen activation and the existence of the Brønsted–Evans–Polanyi (BEP) relationship between the dissociation energy and the adsorption energy of N_2 on $\text{Co}_3\text{Mo}_3\text{N}$ have been clearly shown.^{10,11} The high activity has been attributed to the intermediate adsorption energy of the CoMo phase, as pure Mo adsorbs N_2 too strongly and pure Co adsorbs N_2 too weakly, placing the alloy at the top of the volcano curve close to Ru.^{8,10} Elucidation of a Mars–van Krevelen mechanism on these materials has not yet been considered (see Scheme 1), although the participation of N-vacancies has been considered in a recent DFT study of the electrochemical reduction of ammonia on the rocksalt structure of VN and ZrN ¹² and solar-energy driven ammonia synthesis on metal nitrides via a two-step oxidation–reduction process.^{13,14}

Detailed computational DFT studies of the Ru catalytic system have previously been undertaken. Hu et al. modeled part of the Langmuir–Hinshelwood (L–H) mechanism of

Received: July 15, 2015

Revised: September 28, 2015

Published: October 5, 2015

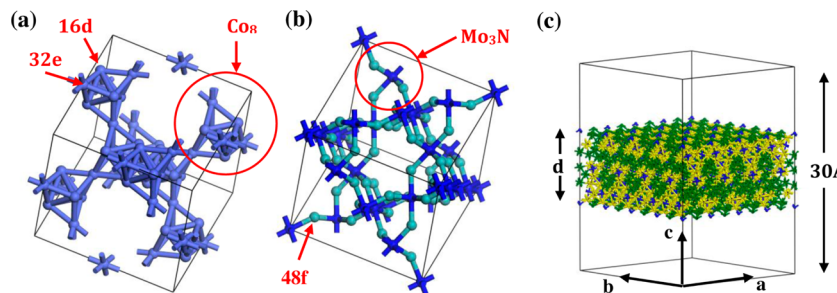
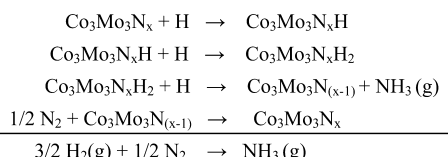


Figure 1. $2 \times 2 \times 2$ bulk supercell of $\text{Co}_3\text{Mo}_3\text{N}$ that has an η -carbide structure belonging to the $\text{Fd}\bar{3}m$ (227) crystal system. Cobalt occupies the Wyckoff sites, 16d and 32e, and the Molybdenum atoms occupy 48f sites. (a) Shows the 3D array of capped at hollow-positions tetrahedra, forming octameric metal nanoclusters (e.g., Co_8), of C_{2v} point group symmetry, (b) the molybdenum nitride framework, and (c) the 4×4 slab model with a primitive hexagonal unit cell belonging to the $\text{P}\bar{3}ml$ (164) crystal system. Defects were chosen to maximize the point group symmetry that was C_{2h} and C_{2v} for the defect-free and defect-containing slabs. We note that the (111)-surface has the highest density of Co_8 clusters embedded in a Mo_3N framework than any other lower symmetry Miller indices. Mo: turquoise. N: blue. Co: purple.

Scheme 1. Hypothetical Mars–van Krevelen Mechanism for Ammonia Synthesis on $\text{Co}_3\text{Mo}_3\text{N}$



ammonia synthesis on Ru [0001] surfaces and steps and showed that the stepwise addition of hydrogen to coadsorbed nitrogen has lower activation barriers, at steps.¹⁵ A compete L–H mechanism was published by Nørskov et al. that showed that the highest activation barrier is the dissociation of N_2 on Ru, which is lower at steps.¹⁶ In particular, it was shown that the mechanism is structure sensitive, because N_2 -activation/dissociation happens more easily at B5 sites.¹⁷ A detailed computational study of the active sites of N_2 dissociation on Ru has been performed by van Santen and co-workers.¹⁸ In the case of $\text{Co}_3\text{Mo}_3\text{N}$, evidence of a Mars–van Krevelen mechanism comes from experiments that show that it can be regenerated from the reduced $\text{Co}_6\text{Mo}_6\text{N}$ phase by the reaction of either N_2 alone or with a N_2/H_2 reaction mixture.^{19,20} Furthermore, isotopic exchange studies showed that the lattice-N in $\text{Co}_3\text{Mo}_3\text{N}$ is exchangeable at elevated temperatures.²¹ Here we aim to offer further support for a Mars–van Krevelen type mechanism on $\text{Co}_3\text{Mo}_3\text{N}$ (111)-nitrogen via accurate periodic DFT calculations. Our aim is to examine if N-vacancies are present in appreciable concentrations on these materials and if molecular nitrogen can adsorb to them and become activated. We therefore calculate the vacancy formation free energy (ΔG_v) and vacancy concentration ($C_{v,\max}^e$) in a T/P range relevant to ammonia synthesis.

In section 3.1, we establish the computational methodology within periodic DFT calculations that should be adopted for ammonia synthesis modeling by exploring various XC-functionals, k-point mesh densities, and planewave cutoff energies.

We then, in section 3.2 calculate the vacancy formation energy (VFE), the vacancy formation free energy, and the equilibrium concentrations of N-vacancies on all nitrogen-containing (111)-surfaces of $\text{Co}_3\text{Mo}_3\text{N}$. Lastly, in section 3.3 we calculate the adsorption energy of N_2 to the various nitrogen-vacancy sites and check whether the $\text{N}\equiv\text{N}$ bond becomes considerably activated and whether this is correlated to the VFE.

2. COMPUTATIONAL METHODOLOGY AND PARAMETERS

Spin-polarized periodic HF, GGA and hybrid-GGA calculations have been performed with the use of the VASP 5.3.5^{22,23} code. Various XC-functionals (i.e., PBE,^{24,25} PW91,^{26,27} PBEsol,²⁸ revPBE,²⁹ B3LYP,^{30,31} HSE06,³² PBE0^{33,34}) and the HF method commonly used for solids and molecular systems have been tested. For the $2 \times 2 \times 2$ bulk supercell of $\text{Co}_3\text{Mo}_3\text{N}$ and the $3 \times 3 \times 3$ supercell of the metallic systems, Co-fcc and Mo-bcc, a Monkhorst–Pack³⁵ k-point grid of $11 \times 11 \times 11$ and $15 \times 15 \times 15$ centered at the Γ -point, respectively, was used (see Supporting Information, Figure S1 and Table S1 for convergence test results). This resulted in convergence of the total energy to less than 0.001 eV (see Table S1). All calculations were performed within the generalized gradient approximation (GGA) with the projector augmented-wave (PAW) method^{36,37} being used to represent the core states. For the optimization algorithm, we employed the residual minimization method with direct inversion in the iterative space (RMM-DIIS). For the metallic systems, we used the following experimental lattice parameters: Co/fcc (10.864 Å)³⁸ and Mo/bcc (9.408 Å)³⁹ that after minimization of the forces on atoms and unit cell with revPBE became 10.648 and 9.521 Å, respectively. For the $\text{Co}_3\text{Mo}_3\text{N}$ ($\text{Fd}\bar{3}m$) crystal, we used the lattice parameter determined by powder neutron diffraction (PND) at 4.2 K¹⁹ of 10.981 Å that after minimization of the forces on atoms and unit cell with revPBE became 11.077 Å, which is an acceptable agreement. The cutoff energy for the plane-wave expansion was set to 650 eV, and the convergence criteria for the ionic and electronic loops were set to 10^{-4} eV and 5×10^{-3} eV·Å⁻¹, respectively, which resulted in residual forces on the atoms < 0.015 eV·Å⁻¹. The initial charge density was obtained by superposition of atomic charges, and the projection operators were evaluated in reciprocal space. Vibrational frequencies were calculated with the finite-difference (FD) method with a 5-point parabola obtained at 0.01 Å increments for the $\text{N}\equiv\text{N}$ bond coordinate. To model the surfaces of the material, a 2×2 slab was used with a vacuum gap of about 22 Å. The slabs were parallel to the (111) surface which is the highest density of the mixed CoMo phase (see Figure 1c) and has previously been associated with the catalytically active surface of $\text{Co}_3\text{Mo}_3\text{N}$ for ammonia synthesis, due to the intermediate binding energy of N_2 to the surface.⁸ An illustration of a 4×4 surface slab similar to the ones used to determine VFEs and adsorption energies is shown in Figure 1c.

Table 1. Theoretical and Experimental Bond Dissociation Enthalpy ($\Delta H_0^\circ(N\equiv N)$), Zero-Point Vibrational Energy (ZPV), and Vibrational Frequency (ν_{N-N}) of $N_2(g)$ in a 20 Å Cube with a Planewave Cut-off of 650 eV for Various XC Functionals (i.e., PBE, PW91, revPBE, PBE0, B3LYP, HSE06) and the HF Method

property	PBE	PW91	revPBE	PBE0	B3LYP	HSE06	HF	Exp.	ref.	units
BDE ^a	1003	1025	959	924	941	920	453			$\text{kJ}\cdot\text{mol}^{-1}$
ZPV ^b	14.4	14.5	14.3	15.2	15.1	15.2	16.6	14.1	40	$\text{kJ}\cdot\text{mol}^{-1}$
$\Delta_{0k}H(N\equiv N)^c$	989	1010	944	909	926	904	436	941.69	41	$\text{kJ}\cdot\text{mol}^{-1}$
ν_{N-N}^d	2415	2425	2390	2542	2521	2540	2782	2359	42	cm^{-1}
MAPE ^e	3.3	4.3	1.1	6.3	5.1	6.4	35.5			%

^aBDE = Bond dissociation energy at 0 K calculated from 2·E(N)–E(N_2). ^bZPV = Zero-point vibrational energy calculated from $h\nu/2$ where ν the stretching frequency of the $N\equiv N$ bond. ^cBond dissociation enthalpy given by $\Delta H_0(N\equiv N) = \text{BDE} - \text{ZPV}$. ^dFrom finite difference method with a displacement of 0.01 Å and a 10^{-7} eV threshold for electronic convergence. ^eAv. MAPE calculated based on eq 1.

3. RESULTS AND DISCUSSION

3.1. Computational Method for Ammonia Synthesis.

The use of DFT in modeling chemical reactions of catalysts has become very popular during the past two decades. Certain limitations, which are related mostly to the accuracy of the various XC-functionals in DFT in estimating activation barriers for elementary surface reactions, suggest that the careful testing of XC-functional, k-point mesh density, and kinetic energy cutoff for the planewave expansion is necessary. We have therefore undertaken a systematic assessment of the aforementioned parameters for ammonia synthesis reactants and surfaces of $\text{Co}_3\text{Mo}_3\text{N}$. In particular, we have calculated for N_2 , the bond dissociation energy (BDE), the zero-point vibrational (ZPV) energy, and the bond dissociation enthalpy (ΔH_{298}°) at 298 K (see Table 1) in order to find the XC-functional that yields accurate thermochemical values. N_2 is one of the main reactants in ammonia synthesis, and accurate prediction of BDEs dictates the accuracy of activation barriers when modeling the reaction mechanism. Since the $N\equiv N$ bond has the highest activation energy barrier in the L–H mechanism for ammonia synthesis on Ru(0001)¹⁶ with our detailed testing of various XC-functionals, we anticipate obtaining greater accuracy in the future development of a kinetic model of ammonia synthesis on $\text{Co}_3\text{Mo}_3\text{N}$. Therefore, we have tested the HF method, various GGA (PBE, PW91, PBE_{sol}) and hybrid-GGA (i.e., PBE0, HSE06, B3LYP) XC-functionals for N_2 in a 20 Å periodic box to avoid spurious interactions between molecule/atoms in adjacent cells. This resulted in converged total energies to less than 0.1 $\text{kJ}\cdot\text{mol}^{-1}$. A test of the interactions of 2 N atoms revealed that their interaction is less than 0.1 $\text{kJ}\cdot\text{mol}^{-1}$ when separated by more than 14 Å. This separation was used as the minimum vacuum gap in our period slab calculations in the following sections, and reported energies have a precision of 0.1 $\text{kJ}\cdot\text{mol}^{-1}$. The calculated physical properties have been compared to experimental values, and the mean-absolute-percentage-error (MAPE) is reported for each property (see Table 1). We have scored the various XC-functionals using an alternative definition of the statistical MAPE that has an average in the denominator given by

$$\text{MAPE} = \frac{100\%}{N} \sum_{i=1}^N \left| \frac{(x_{\text{exp}} - x_{\text{calc}})}{(x_{\text{exp}} + x_{\text{calc}})/2} \right| \quad (1)$$

where N is the number of properties and MAPE is a quantitative measure of agreement between experiment and theory. This MAPE gives a more representative measure of the percentage difference between experiment and calculation especially when there is a large difference between the two (e.g., MAPE for HF).

In Table 1 we present the calculated, the theoretical, and experimental bond dissociation enthalpy ($\Delta H_0^\circ(N\equiv N)$), zero-point vibrational energy (ZPV), and vibrational frequency (ν_{N-N}) of $N_2(g)$ for various XC-functionals (i.e., PBE, PW91, revPBE, PBE0, B3LYP, HSE06) and the HF method. These results clearly show that the two GGA functionals commonly used to model surface reactions (i.e., PBE, PW91) overestimate the $\Delta H_0^\circ(N\equiv N)$ of N_2 by 47 $\text{kJ}\cdot\text{mol}^{-1}$ (+5.0%) and 68 $\text{kJ}\cdot\text{mol}^{-1}$ (+7.2%), respectively. The Hartree–Fock method (HF) fails dramatically by more than 500 $\text{kJ}\cdot\text{mol}^{-1}$ showing that the inclusion of electron correlation is crucial for improving the estimation of thermochemical properties. It is generally known that errors in GGA atomization energies are most severe for multiply bonded molecules such as N_2 due to errors in the exchange limit.²⁸ We find that the revised version of the PBE functional (revPBE) yields a calculated bond dissociation enthalpy to within 2 $\text{kJ}\cdot\text{mol}^{-1}$ of the spectroscopic value. Additionally it estimates the vibrational stretching frequency of the $N\equiv N$ bond (ν_{N-N}) to within 1.3%. These results are exceptionally good, as in a recent extensive account of XC-functionals that included meta-GGA, hybrid meta-GGA, and range-separated hybrid GGA, it has been shown that even with state-of-the-art XC-functionals the errors remain about 15 $\text{kJ}\cdot\text{mol}^{-1}$ for BDEs and bond-dissociation activation barriers.⁴³ We anticipate that this careful consideration of various XC-functionals should improve the computational accuracy of our study.

We additionally investigated whether the use of atom-centered functions (Gaussian type functions) rather than planewaves would affect the choice of XC-functional, due to potential changes at the cusp and the long-range tails of the wave functions being modeled via the two methods. Therefore, we have compared the calculated BDEs using planewaves with results obtained in a code that uses atom centered-basis sets (i.e., G09⁴⁴), using the cc-pVTZ and cc-pVQZ (see Figure S2) basis sets, and found that the BDE for the latter are 15–20 $\text{kJ}\cdot\text{mol}^{-1}$ higher. There the hybrid XC-functionals (PBE1PBE ≡ PBE0, B3LYP, HSEh1PBE ≡ HSE06) generally performed better than the GGA functionals (PBEPBE ≡ PBE, PW91PW91 ≡ PW91), and especially the B3LYP functionals gave the lowest average MAPE. This finding is in agreement with an assessment study of the PBE0 functional, where it was shown to be as good as the B3LYP functional for predicting the atomization energies of the G2 set, whereas the PBE functional appears to have systematic errors.⁴⁵ It is therefore evident that a case-based screening of XC functionals is still necessary for the computational modeling of surface reactions and that a different test is necessary when switching from a planewave code to an atom-centered code and vice versa. Since for the

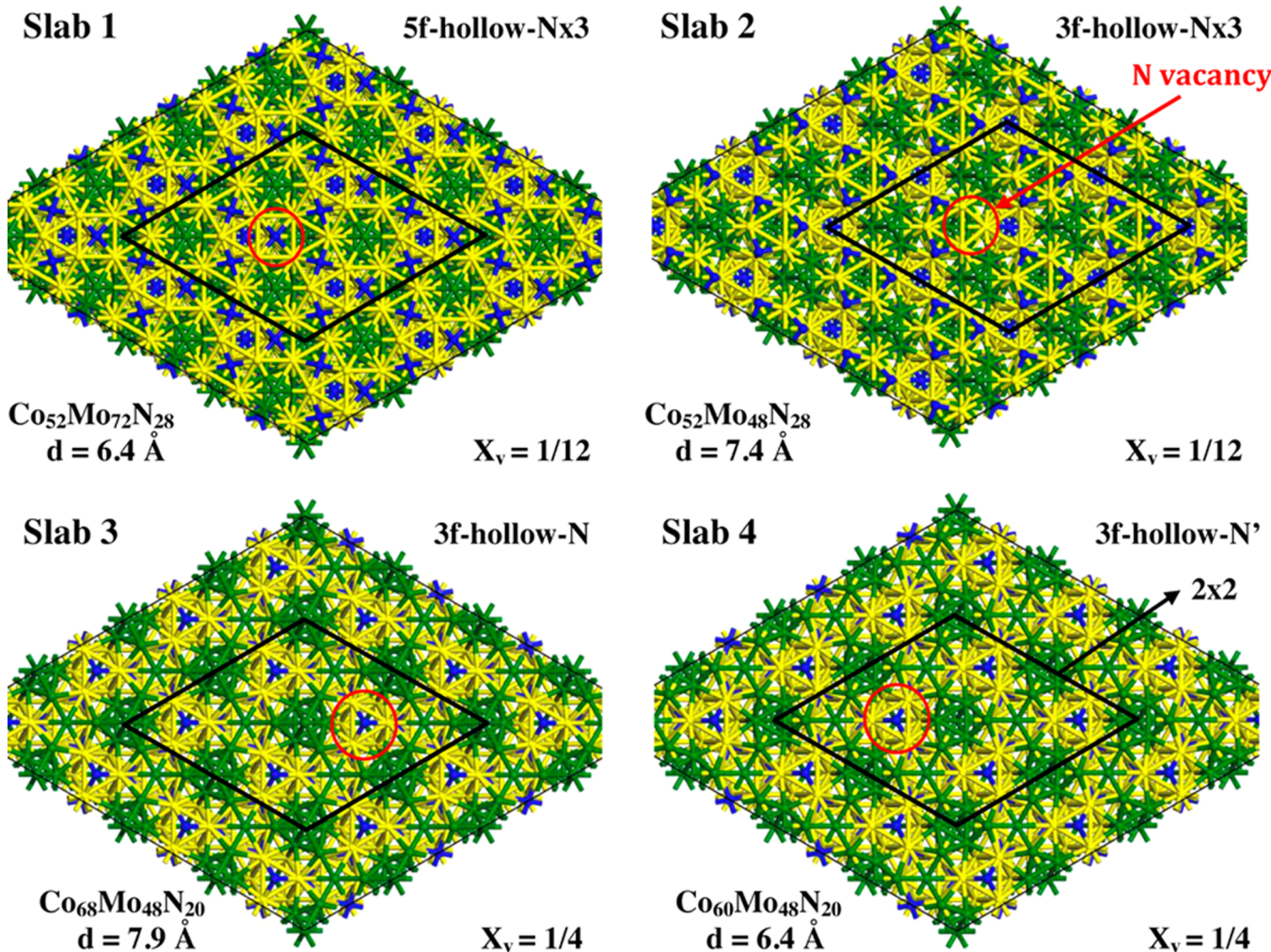


Figure 2. 2×2 surface unit cells of the different surface nitrogen-containing (111)-surfaces of $\text{Co}_3\text{Mo}_3\text{N}$ ($\text{Co}: \text{Mo} \neq 1:1$) showing the stoichiometric formula, the slab thickness before relaxation, and the molar fraction of vacancies. The defect-free nitrogen surface concentration of slab 1–2 is three times greater than slab 3–4, and their corresponding nitrogen-vacancy surface molar fractions, $X_{v,1x1}$ and $X_{v,2x2}$, are shown. The length of the 1×1 and 2×2 surface vector was 7.832 and 15.665 Å, respectively. Two surface slabs that had no nitrogen exposed are presented in the Supporting Information (see Figure S3). Mo: yellow. N: blue. Co: green.

remaining calculations we have used a planewave code, we have adopted the revPBE XC-functional with a 650 eV cutoff for the planewave expansion.

3.2. Nitrogen Vacancy-Formation Energies and Con-

centrations. It is evident from the schematic of a Mars-van Krevelen mechanism shown in Scheme 1 and the very large bond dissociation enthalpy of N₂ (941 kJ·mol⁻¹), for the activation of dinitrogen, that nitrogen vacancies are necessary which could potentially lower the barrier for nitrogen activation (i.e., weakening and elongation of the N≡N bond), as with the activation of other multiple bonded molecules at oxygen surface vacancies (e.g., oxidation of CO over CeO₂,⁴⁶ methanol synthesis over Cu/ZnO,⁴⁷ activation of CO₂ on ZnO⁴⁸). Therefore, we have calculated the N-VFEs and the corresponding equilibrium vacancy concentrations for Co₃Mo₃N particles, which have not been reported so far in the literature. We have tested two ways of calculating the VFE which are described below. The nitrogen VFE is calculated as the difference between the energy of the slab before and after introduction of a surface vacancy to which we have added half the energy of N₂ optimized alone in a 20 Å cubic cell. We calculate the single and double (on opposing sites of the slab) nitrogen VFEs on every

nitrogen containing the (111)-surface of $\text{Co}_3\text{Mo}_3\text{N}$ shown in Figure 2.

In order to find the various surface terminations of $\text{Co}_3\text{Mo}_3\text{N}$ we have used a scanning algorithm. The slab models of the (111) surface of $\text{Co}_3\text{Mo}_3\text{N}$ were generated by (a) scanning the z value of an (11 z)-plane in $\Delta z = 0.1 \text{ \AA}$ increments between 0 and 1. This generated six different surface terminations of which the four contained surface nitrogen (i.e., surface 1). Once the composition unique surface was identified we then (b) searched for the closest (11 z)-plane with the same surface composition (surface 2). We then (c) used the bulk geometry that was enclosed between the two surfaces (surface 1 and surface 2) and used it for the slab model. This resulted in slabs that had a slab thickness (d_i) in the range of 6.4–7.9 \AA . We note that these nanofilms of $\text{Co}_3\text{Mo}_3\text{N}$ would acquire a slightly different thickness after relaxation, the change of which was small enough that the slab model is a good representation of the surface of a bulk material. This is evident from the <10% percentage relaxation of the slab equilibrium lattice spacing that we observed, which is similar to the surface relaxation percentage known for Mo(001).⁴⁹ The slab thickness prior to and after relaxation as well as after the nitrogen vacancy

Table 2. Nitrogen Vacancy-Formation Energy Per Nitrogen ($VFE_{N_{vac}}$), Vacancy Equilibrium Concentrations ($C_{v,max}^e(T)$) at 25 and 379 °C, N₂ Adsorption Energy (ΔE_{ads}), Surface Formation Energy (E_s^F), Mo–N Bond Length ($r_{(Mo-N)}$) and Slab Thickness (d_{slab}) for the Bulk (2 × 2 × 2) Unit Cell of Co₃Mo₃N and Four Nitrogen Containing (111)-Surfaces of Co₃Mo₃N^a

property	(2 × 2 × 2)	5f-hollow-N×3	3f-hollow-N×3	3f-hollow-N	3f-hollow-N'	units
stoichiometry	Co ₃ Mo ₃ N	Co ₅₂ Mo ₇₂ N ₂₈	Co ₅₂ Mo ₄₈ N ₂₈	Co ₆₈ Mo ₄₈ N ₂₀	Co ₆₀ Mo ₄₈ N ₂₀	—
defect type	5f	5f	3f	3f	3f	—
$VFE_{(2 \times 2)}\text{-}1N_{vac}$	(1.49) ^b	—	—	1.52	1.41	eV
$VFE_{(1 \times 1)}\text{-}2N_{vac}$	—	2.34	1.63	1.51	1.38	eV
$VFE_{(2 \times 2)}\text{-}2N_{vac}$	—	2.35 ^c	1.68	1.48	1.39	eV
$C_{v,max}^e(25\text{ }^\circ\text{C})$ ^d	(1.7 × 10 ¹⁵)	8.8 × 10 ¹⁴	2.6 × 10 ¹⁵	1.7 × 10 ¹⁴	2.6 × 10 ¹⁴	mol ⁻¹
$C_{v,max}^e(379\text{ }^\circ\text{C})$	(1.5 × 10 ¹⁶)	8.1 × 10 ¹⁵	1.3 × 10 ¹⁶	1.3 × 10 ¹⁶	1.6 × 10 ¹⁶	mol ⁻¹
ΔE_{ads}^e	—	48.7	-19.6	62.0	65.7	kJ·mol ⁻¹
E_s^F	—	0.64	9.27	8.61	10.33	J·m ⁻²
$r_{(Mo-N)}$	—	2.120	1.930	1.976	1.971	Å
$d_{slab,initial}^f$	—	7.37	6.39	7.89	6.40	Å
$d_{slab,relaxed}$	—	6.67	6.42	7.63	6.11	Å
$d_{slab,Nvac}$	—	6.65	6.48	7.81	6.11	Å

^aProperties calculated using the revPBE XC-functional and $E_{cut} = 650$ eV. We used a Monkhorst–Pack k-point mesh centered at the Γ -point, with $8 \times 8 \times 1$ and $4 \times 4 \times 1$ k-points, for the (1 × 1) and (2 × 2) surface units cells, respectively. ^bParentheses indicate that the reported values are hypothetical as the nitrogen diffusion pathway is sterically hindered. ^cVFE shown in bold were used to calculate the equilibrium vacancy concentrations using eq 3. ^dConcentration determined based on the maximum surface area of Co₃Mo₃N catalyst that ranges between 8 and 21 m²/g. ^eThe adsorption energy of nitrogen was based on the adsorption of two nitrogen molecules on opposing sites of the slab. ^fDetermined based on the distance of the center-of-mass of two Mo atoms on opposing surfaces of the relaxed slabs.

formation are given in Table 2. Lastly, (e) the surface slab enclosed between the composition unique surfaces was then translated along the *c*-vector (*x*, *y*, 15 Å) until the slab was at the center of the hexagonal unit cell, which maximized the point group symmetry to C_{2h} and enhanced the computational efficiency of the calculations.

Our algorithm for obtaining slabs (i.e., thin films) of Co₃Mo₃N show that the various nitrogen-containing surfaces of Co₃Mo₃N exhibit two types of surface-bound nitrogen (i.e., 3f-hollow and 5f-hollow) simply denoted as 3f and 5f, based on their coordination number. The 3f-hollow corresponds to tetrahedrally bound nitrogen, and the 5f-hollow, to square-pyramidal bound nitrogen where nitrogen occupies the center-of-square. Although the surface slabs were allowed full relaxation, there was a complete absence of surface reconstruction; however there was a small contraction of the slab thickness, ranging between 3.3% to 9.5% (see Table 2). Although the introduction of vacancies and defects in general at surfaces usually causes the surface to expand, we observe that in nanofilms of cobalt molybdenum nitrides the introduction of vacancies can cause both expansion (e.g., 3f-hollow-N×3, 3f-hollow-N) and contraction (e.g., 5f-hollow-N×3) of the slab thickness which is however very small (<2.3%).

For the calculation of VFE for nitrogen and the corresponding vacancy concentrations, we have performed calculations where the surface model has a neutral charge. Therefore, spurious intra- and interlayer electrostatic interactions of charged defect sites are not present in our calculations and in the reported VFEs.⁵⁰ In fact we show that interactions between nitrogen vacancies on Co₃Mo₃N are negligible by calculating both the interlayer and intralayer interaction by considering surface unit cells of varying size (i.e., 1 × 1 and 2 × 2) and slabs with single and double vacancies on opposing surfaces of the slab, so that two nitrogen vacancies can directly interact through a vacuum. These systematic calculations show that the interlayer interaction is less than 0.03 eV per vacancy pair and the intralayer interaction at low nitrogen vacancy coverage ($X_v = 1/12$) is less than 0.04 eV,

energies below the thermal energy at the average temperature used for ammonia synthesis (450 °C, 0.06 eV). Therefore, any correction schemes for spurious interactions between periodic images were not necessary and the computational accuracy of the VFEs we present is of the order of 0.05 eV. The VFEs were then used to estimate via a semiempirical treatment in order to calculate the free energy of vacancy formation (ΔG_v). This can yield the nitrogen vacancy concentrations as a function of temperature, a value very useful in order to quantify the number of active sites on Co₃Mo₃N catalysts that can potentially activate N₂.

In order to calculate surface vacancy concentrations, we have calculated vacancy formation free energies by explicitly taking into account vacancy configurational entropy and entropic contributions due to N₂ in the temperature and pressure range for ammonia synthesis, taken from thermodynamic tables according to the following formula (a detailed derivation is given in the Supporting Information),

$$\Delta G_v \cong \Delta E_v X_v - T \Delta S_v(T) X_v + RT[(X_v \ln X_v + (1 - X_v) \ln(1 - X_v))] \quad (1)$$

The temperature-dependent entropy change of molecular N₂ at 98.7 atm, which is at the lower threshold for ammonia synthesis, was calculated by linear fitting of the following thermodynamic values that were measured at 98.7 atm: $S_{300\text{ K}} = 151.7 \text{ J}\cdot\text{mol}^{-1}$, $S_{400\text{ K}} = 161.0 \text{ J}\cdot\text{mol}^{-1}$, and $S_{500\text{ K}} = 167.9 \text{ J}\cdot\text{mol}^{-1}$.⁵¹ The equilibrium vacancy molar fraction at temperature T was calculated according to

$$X_v^e(T) = g \cdot \exp\left(\frac{-\Delta G_v}{RT}\right) \quad (2)$$

where g is a degeneracy factor accounting for internal degrees of freedom of the point defect.⁵² The equilibrium vacancy concentrations were calculated using

$$C_v^e(T) = \frac{N_{Av}}{\text{MW} \cdot S} X_v^e(T) \quad (3)$$

where S is the specific surface area per mass ($8\text{--}21\text{m}^2\text{g}^{-1}$), N_{Av} , Avogadro's number, and MW, the molar mass of $\text{Co}_3\text{Mo}_3\text{N}$.

The slab formation energy per unit area (E_s^F) was calculated according to the equation

$$E_s^F = (E_{\text{slab},\text{CoxMoyN}} - xE_{\text{Co}} - yE_{\text{Mo}} - zE_{\text{N}})/2A \quad (4)$$

where A is the area of the surface unit cell; $E_{\text{slab},\text{CoxMoyN}}$, E_{Co} , E_{Mo} , and E_{N} are the total energies of the slab and the elements calculated from bulk Co-fcc($2 \times 2 \times 2$), Mo-bcc($2 \times 2 \times 2$), and N_2 in a 20 Å periodic cube, respectively; and x , y , z are the stoichiometric coefficients of the slab's elemental formula shown in Table 2.

According to the slab formation energy calculations presented in Table 2, we find that the 3f surfaces (i.e., 3f-hollow-N, 3f-hollow-N×3, 3f-hollow-N') have generally higher slab surface energies (8.61 to 10.33 J·m⁻²) compared to the 5f that has a slab formation energy of 0.64 J·m⁻². The relative stability of the various nitrogen-containing surfaces based on these slab formation energies were found to have the order 5f-hollow-N×3 > 3f-hollow-N > 3f-hollow-N×3 > 3f-hollow-N', and we suggest that they can be used to rank the relative abundance of the various surface terminations on the $\text{Co}_3\text{Mo}_3\text{N}$ nanoparticles. This suggests that, for the nitrogen containing (111)-facets on $\text{Co}_3\text{Mo}_3\text{N}$ catalyst particles, most will have a 5f nitrogen. The latter, however, has the most strongly bound surface nitrogen, with VFEs of 227 kJ·mol⁻¹ compared to 134–162 kJ·mol⁻¹ that the 3f-hollow surfaces have. Therefore, although the 5f-hollow-N×3 is expected to be more abundant on $\text{Co}_3\text{Mo}_3\text{N}$ catalyst particles, it is not expected to contribute substantially to ammonia synthesis via the Mars–van Krevelen type mechanism, due to the large nitrogen-VFE energy that makes the formation of vacancies of this kind highly unlikely in the ammonia synthesis temperature range. In contrast the 3f-hollow surfaces that happen to have higher surface energies appear to be the catalytically relevant surfaces, as their vacancies form at considerably lower temperatures (and at higher concentrations), even as low as 200 °C.

In Figure 3 we show the calculated equilibrium nitrogen vacancy concentration in the temperature range of ammonia synthesis (380–550 °C). We found that it ranges between 1.6×10^{16} and 3.7×10^{16} cm⁻² which is high, if one considers that these are active sites if dinitrogen is able not only to adsorb but also be activated in order to undergo further catalytic reactions. We compare the vacancy concentrations at 25 °C (7.1×10^{13} – 1.9×10^{14} cm⁻²) to a recent Transmission Electron Aberration-Corrected Microscopy (TEAM) study of vacancy concentrations on MoS_2 films. Although the Mo–S bond strength will have a different strength than the Mo–N bond, we find equilibrium vacancy concentrations were found to be of the same order of magnitude (3.5×10^{13} cm⁻²)⁵³ as the ones we report here for the first time.

3.3. Nitrogen Adsorption and Activation at Vacancy Sites.

Here we examine whether N_2 can adsorb and become activated at nitrogen vacancies formed on $\text{Co}_3\text{Mo}_3\text{N}$ (111) surfaces. The adsorption studies were done in the following fashion: we have placed N_2 molecules perpendicularly to the surface at the center of the square and the triangle of the corresponding 5f and 3f vacancies. The nitrogen atom that was closer to the surface was in the same plane as the surrounding Mo atoms, and the whole surface/adsorbate system was allowed

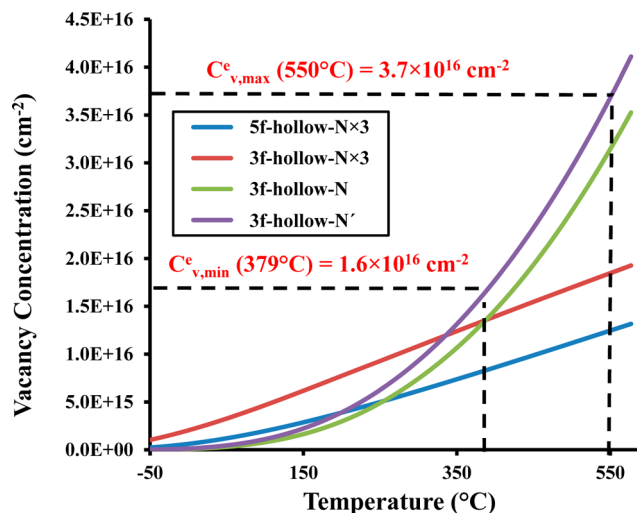


Figure 3. Nitrogen-vacancy concentration as a function of temperature on all nitrogen-containing (111)-surfaces of $\text{Co}_3\text{Mo}_3\text{N}$. Dashed lines correspond to the usual temperature range of ammonia synthesis. Curves obtained using eq 3.

to relax without constraints. Thus, the nitrogen could either desorb or adsorb by elongation of the N–N bond. Although we anticipated exothermic adsorption energies for N_2 at vacancies (see Table 2, ΔE_{ads}), we found that most of the adsorption energies are endothermic apart from one surface, indicative of a considerable electronic reconstruction of the surfaces when N-vacancies were formed. The only surface that preserved the number of unpaired electrons at the vacancy sites and gave exothermic adsorption energies ($-19.6 \text{ kJ}\cdot\text{mol}^{-1}$) for N_2 was the 3f-hollow-N×3 surface which is in general agreement with the values found from kinetic modeling of ammonia synthesis¹¹ and earlier DFT calculations.⁸ The other three surfaces (5f-hollow-N×3, 3f-hollow-N×3, 3f-hollow-N') gave significantly high endothermic adsorption energies for N_2 that range between 49 to 66 kJ·mol⁻¹. Based on the DFT calculated adsorption energies, the surface formation energies, and the nitrogen vacancy concentrations, we have found that the most probable surface where the Mars–van Krevelen chemistry may happen is the 3f-hollow-N×3 surface of $\text{Co}_3\text{Mo}_3\text{N}$ nanoparticles. This surface will be used in future work to model the Mars–van Krevelen mechanism for ammonia synthesis on $\text{Co}_3\text{Mo}_3\text{N}$ and compare it to the L–H mechanism, the dominant catalytic mechanistic pathway found for Ru[0001] surfaces.

In these studies, the activation of nitrogen is considered to be the most difficult mechanistic step for ammonia synthesis on both Ru and Fe surfaces.^{10,16} The effect of strain on the activation barrier on iron surfaces showed that it can be lowered by expanding the lattice parameter.⁵⁴ In another study of the activation of multiple-bonded molecules, van Santen and co-workers showed that H-assisted dissociation lowers the barrier for CO activation on Ru in the Fischer–Tropsch mechanism.⁵⁵ Nonetheless a recent study by Iglesia and co-workers shows that although H-assisted dissociation of multiply bonded molecules (e.g., CO, NO, O₂) lowers the activation barrier this does not happen in the case of N₂ on Ru[0001].⁵⁶

In Figure 4 we present the calculated N₂ bond lengths for the molecule adsorbed at the different vacancy sites which we correlate with the VFE. We find that both 3f-hollow and 5f-hollow nitrogen vacancies can activate N₂ by weakening

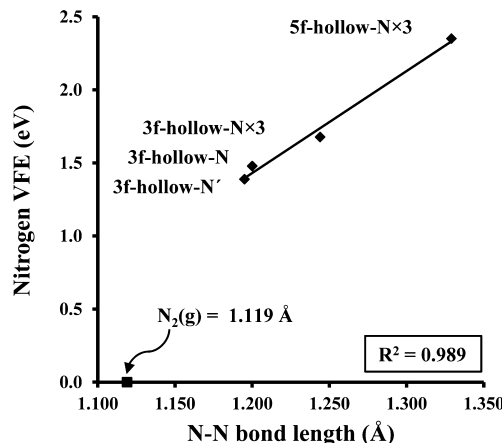


Figure 4. Nitrogen VFE as a function of the bond length in activated molecular nitrogen adsorbed to nitrogen vacancies compared to N_2 in vacuum.

considerably the $\text{N}\equiv\text{N}$ bond evident from the large increase in the $\text{N}\equiv\text{N}$ bond length. The percentage increase of the $\text{N}\equiv\text{N}$ bond length due to adsorption/activation at vacancies was found to be 18.8%, 7.2%, 11.2%, and 6.8% for **5f-hollow-N \times 3**, **3f-hollow-N**, **3f-hollow-N \times 3**, **3f-hollow-N'**, respectively. Figure 4 shows that the bond length increase is roughly proportional to the VFE, clearly suggesting that vacancy sites that require more energy to be formed can activate nitrogen more effectively. The interpretation of this phenomenon can be based on the Dewar–Chatt–Duncanson bonding model that rationalizes the activation of an end-on bound N_2 in transition metal complexes. In that, the filled N_2 nonbonding σ -orbital forms a dative bond with empty metal d_{z^2} or $d_{x^2-y^2}$ orbitals and the filled d_{xz} , d_{yz} , or d_{xy} orbital of the transition metal donates electron density into the $2\pi^*$ antibonding orbitals of N_2 via π -backdonation. This backdonation weakens the N–N bond, effectively activating the ligand, which requires less energy for subsequent bond dissociation reactions. Since the energy required to remove a single N atom from the surface of $\text{Co}_3\text{Mo}_3\text{N}$ is proportional to the energy required to remove molecular nitrogen that is bound end-on as shown in an earlier study,⁵⁴ this means that the stronger N_2 is bound the more π -backdonation occurs which weakens the $\text{N}\equiv\text{N}$ bond (i.e., adsorption-induced bond-elongation). Figure 4 clearly shows that the VFE energy is therefore linearly proportional to the N–N bond length. It is therefore suggested that the VFE in combination with the adsorption energies can be used as a descriptor for the screening of materials that can adsorb and activate double or triple bonded molecules (e.g., O_2 , N_2 , CO, NO) that are bound end-on at surface vacancies. This result is intriguing, as it reduces the computational problem of screening materials to a single-point energy calculation.

4. SUMMARY AND CONCLUSIONS

In summary, we present for the first time nitrogen-vacancy formation free energies and concentrations for conditions relevant to ammonia synthesis (380 to 550 °C, 100 atm) over $\text{Co}_3\text{Mo}_3\text{N}$. We have explicitly considered the configurational entropy and the temperature-dependent entropic contributions due to N_2 at 100 atm via a semiempirical approach. We observe that two types of nitrogen vacancies exist, 3f and 5f vacancies, with vacancy formation energies in the range of 1.39 to 2.35 eV. We determine that the 3f-nitrogen containing surfaces that

form N-vacancies more easily have surprisingly high concentrations (1.6×10^{16} to $3.7 \times 10^{16} \text{ cm}^{-2}$) at conditions relevant to ammonia synthesis. The catalytically active surface that we find is the **3f-hollow-N \times 3** that resembles the structure of a bifunctional catalyst, as the nitrogens bound to the molybdenum framework coexist with a hexagonal array of embedded Co_8 nanoclusters.

We report for the first time that the VFE in combination with the adsorption energy can be used as a descriptor in the screening of materials that activate multiple-bound molecules such as N_2 . This significantly reduces the computational cost for the computational screening of materials, as only a single-point energy calculation is required for each material once the chemical potential of consisting elements is known.

■ ASSOCIATED CONTENT

S Supporting Information

The Supporting Information is available free of charge on the ACS Publications website at DOI: 10.1021/acs.jpcc.5b06811.

The k-point mesh convergence test (Figure S1, Table S1); BDE for N_2 using the cc-pVTZ and cc-pVQZ basis sets (Figure S2); in Figure 2 the two surface slabs that had no nitrogen exposed (Figure S3) (PDF)

■ AUTHOR INFORMATION

Corresponding Authors

*E-mail: c.zeinalipour-yazdi@ucl.ac.edu. Tel: +44 207-679-0312.

*E-mail: c.r.a.catlow@ucl.ac.edu. Tel: +44 207-235-2818.

Notes

The authors declare no competing financial interest.

■ ACKNOWLEDGMENTS

The authors acknowledge EPSRC funding through EP/L026317/1 and via our membership of the UK's HEC Materials Chemistry Consortium, which is funded by EPSRC (EP/L000202); this work used the ARCHER UK National Supercomputing Service (<http://www.archer.ac.uk>). The authors acknowledge Dr. Furio Cora and Dr. Andrew Logsdail for useful discussions and the support of UCL's Research Computing team with the use of the ib-server@UCL.

■ REFERENCES

- (1) FAOSTAT, World cereal production and fertilizer consumption 1971–2007. In *IFA statistics*, 2008.
- (2) Smil, J. Detonator of the population explosion. *Nature* **1999**, *400*, 415–415.
- (3) Jennings, J. *Catalytic ammonia synthesis: fundamentals and practice*; Plenum: New York, 1991.
- (4) Rafiqul, I.; Weber, C.; Lehmann, B.; Voss, A. Energy efficiency improvements in ammonia production—perspectives and uncertainties. *Energy* **2005**, *30*, 2487–2504.
- (5) Jacobsen, C. J. H.; Brorson, M.; Sehested, J.; Teunissen, H.; Törnqvist, E. O. Process for the preparation of ammonia and ammonia synthesis catalyst. US 6,235,676, 1999.
- (6) Kojima, R.; Aika, K.-I. Cobalt molybdenum bimetallic nitride catalysts for ammonia synthesis: Part 1. Preparation and characterization. *Appl. Catal., A: Gen.* **2001**, *215*, 149–160.
- (7) Jacobsen, C. J. H. Novel class of ammonia synthesis catalysts. *Chem. Commun.* **2000**, 1057–1058.
- (8) Jacobsen, C. J. H.; Dahl, S.; Clausen, B. S.; Bahn, S.; Logadottir, A.; Nørskov, J. Catalyst Design by Interpolation in the Periodic Table: Bimetallic Ammonia Synthesis Catalysts. *J. Am. Chem. Soc.* **2001**, *123*, 8404–8405.

- (9) McKay, D.; Hargreaves, J. S. J.; Rico, J. L.; Rivera, J. L.; Sun, X.-L. The influence of phase and morphology of molybdenum nitrides on ammonia synthesis activity and reduction characteristics. *J. Solid State Chem.* **2008**, *181*, 325–333.
- (10) Nørskov, J. K.; Bligaard, T.; Logadóttir, A.; Bahn, S.; Hansen, L. B.; Bollinger, M.; Bengaard, H.; Hammer, B.; Sljivancanin, Z.; Mavrikakis, M.; Xu, Y.; Dahl, S.; Jacobsen, C. J. H. Universality in Heterogeneous Catalysis. *J. Catal.* **2002**, *209*, 275–278.
- (11) Boisen, A.; Dahl, S.; Jacobsen, C. J. H. Promotion of Binary Nitride Catalysts: Isothermal N₂ Adsorption, Microkinetic Model, and Catalytic Ammonia Synthesis Activity. *J. Catal.* **2002**, *208*, 180–186.
- (12) Abghoui, Y.; Garden, A. L.; Hlynsson, V. F.; Bjorgvinsdóttir, S.; Olafsdóttir, H.; Skulason, E. Enabling electrochemical reduction of nitrogen to ammonia at ambient conditions through rational catalyst design. *Phys. Chem. Chem. Phys.* **2015**, *17*, 4909–4918.
- (13) Michalsky, R.; Pfromm, P. H.; Steinfeld, A. Rational design of metal nitride redox materials for solar-driven ammonia synthesis. *Interface Focus* **2015**, *5*, 20140084.
- (14) Michalsky, R.; Avram, A. M.; Peterson, B. A.; Pfromm, P. H.; Peterson, A. A. Chemical looping of metal nitride catalysts: low-pressure ammonia synthesis for energy storage. *Chem. Sci.* **2015**, *6*, 3965–3974.
- (15) Zhang, C. J.; Lynch, M.; Hu, P. A density functional theory study of stepwise addition reactions in ammonia synthesis on Ru(0 0 0 1). *Surf. Sci.* **2002**, *496*, 221–230.
- (16) Logadóttir, A.; Nørskov, J. Ammonia synthesis over a Ru(0001) surface studied by density functional calculations. *J. Catal.* **2003**, *220*, 273–279.
- (17) Jacobsen, C. J. H.; Dahl, S.; Hansen, P. L.; Törnqvist, E.; Jensen, L.; Topsøe, H.; Prip, D. V.; Møenshaug, P. B.; Chorkendorff, I. Structure sensitivity of supported ruthenium catalysts for ammonia synthesis. *J. Mol. Catal. A: Chem.* **2000**, *163*, 19–26.
- (18) Shetty, S.; Jansen, A. P. J.; van Santen, R. A. Active Sites for N₂ Dissociation on Ruthenium. *J. Phys. Chem. C* **2008**, *112*, 17768–17771.
- (19) Hunter, S. M.; McKay, D.; Smith, R. I.; Hargreaves, J. S. J.; Gregory, D. H. Topotactic Nitrogen Transfer: Structural Transformation in Cobalt Molybdenum Nitrides. *Chem. Mater.* **2010**, *22*, 2898–2907.
- (20) Gregory, D. H.; Hargreaves, J. S. J.; Hunter, S. M. On the Regeneration of Co₃Mo₃N from Co₆Mo₆N with N₂. *Catal. Lett.* **2011**, *141*, 22–26.
- (21) Hunter, S. M.; Gregory, D. H.; Hargreaves, J. S. J.; Richard, M. I.; Duprez, D.; Bion, N. A Study of 15N/14N Isotopic Exchange over Cobalt Molybdenum Nitrides. *ACS Catal.* **2013**, *3*, 1719–1725.
- (22) Kresse, G.; Furthmüller, J. Efficient Iterative Schemes for *ab initio* Total-Energy Calculations Using a Plane-Wave Basis Set. *Phys. Rev. B: Condens. Matter Mater. Phys.* **1996**, *54*, 11169–11186.
- (23) Kresse, G.; Hafner, J. *Ab initio* Molecular Dynamics for Liquid Metals. *Phys. Rev. B: Condens. Matter Mater. Phys.* **1993**, *47*, 558–561.
- (24) Perdew, J. P.; Burke, K.; Ernzerhof, M. Generalized Gradient Approximation Made Simple. *Phys. Rev. Lett.* **1996**, *77*, 3865–3868.
- (25) Perdew, J. P.; Burke, K.; Ernzerhof, M. Erratum: Generalized gradient approximation made simple. *Phys. Rev. Lett.* **1997**, *78*, 1396.
- (26) Perdew, J. P.; Chevary, J. A.; Vosko, S. H.; Jackson, K. A.; Pederson, M. R.; Singh, D. J.; Fiolhais, C. Erratum: Atoms, molecules, solids, and surfaces: Applications of the generalized gradient approximation for exchange and correlation. *Phys. Rev. B: Condens. Matter Mater. Phys.* **1993**, *48*, 4978.
- (27) Perdew, J. P.; Chevary, J. A.; Vosko, S. H.; Jackson, K. A.; Pederson, M. R.; Singh, D. J.; Fiolhais, C. Atoms, molecules, solids, and surfaces: Applications of the generalized gradient approximation for exchange and correlation. *Phys. Rev. B: Condens. Matter Mater. Phys.* **1992**, *46*, 6671–6687.
- (28) Perdew, J. P.; Ruzsinszky, A.; Csonka, G. I.; Vydrov, O. A.; Scuseria, G. E.; Constantin, L. A.; Zhou, X.; Burke, K. Restoring the Density-Gradient Expansion for Exchange in Solids and Surfaces. *Phys. Rev. Lett.* **2008**, *100*, 136406.
- (29) Zhang, Y.; Yang, W. Comment on “Generalized Gradient Approximation Made Simple. *Phys. Rev. Lett.* **1998**, *80*, 890.
- (30) Becke, A. D. Density-Functional Thermochemistry. III. The Role of Exact Exchange. *J. Chem. Phys.* **1993**, *98*, 5648–5652.
- (31) Lee, C.; Yang, W.; Parr, R. G. Development of the Colle-Salvetti Correlation-Energy Formula into a Functional of the Electron Density. *Phys. Rev. B: Condens. Matter Mater. Phys.* **1988**, *37*, 785–789.
- (32) Krukau, A. V.; Vydrov, O. A.; Izmaylov, A. F.; Scuseria, G. E. Influence of the exchange screening parameter on the performance of screened hybrid functionals. *J. Chem. Phys.* **2006**, *125*, 224106.
- (33) Burke, K.; Ernzerhof, M.; Perdew, J. P. The adiabatic connection method: a non-empirical hybrid. *Chem. Phys. Lett.* **1997**, *265*, 115.
- (34) Adamo, C.; Barone, V. Toward reliable density functional methods without adjustable parameters: The PBE0 model. *J. Chem. Phys.* **1999**, *110*, 6158–6170.
- (35) Monkhorst, H. J.; Pack, J. D. Special Points for Brillouin-Zone Integrations. *Phys. Rev. B* **1976**, *13*, 5188–5192.
- (36) Kresse, G.; Joubert, D. From Ultrasoft Pseudopotentials to the Projector Augmented-Wave Method. *Phys. Rev. B: Condens. Matter Mater. Phys.* **1999**, *59*, 1758–1775.
- (37) Blöchl, P. E. Projector Augmented-Wave Method. *Phys. Rev. B: Condens. Matter Mater. Phys.* **1994**, *50*, 17953–17979.
- (38) Kohlhaas, R.; Dunner, P.; Schmitz-Pranghe, N. Über die temperaturabhängigkeit der gitterparameter von eisen, kobalt und nickel im bereich hoher temperaturen. *Z. Angew. Phys.* **1967**, *23*, 245–249.
- (39) Davey, W. P. Precision Measurements of the Lattice Constants of Twelve Common Metals. *Phys. Rev.* **1925**, *25*, 753–761.
- (40) Irikura, K. K. Experimental Vibrational Zero-Point Energies: Diatomic Molecules. *J. Phys. Chem. Ref. Data* **2007**, *36*, 389–397.
- (41) Wagman, D. D.; Evans, W. H.; Parker, V. B.; Halow, I.; Bailey, S. M.; Schumm, R. H. *Selected values of thermodynamic properties Part 3, Tables for the first thirty-four elements in their standard order of arrangement*; Nat. Bur. Stand. (U.S.) Tech. Note, 1967.
- (42) Shimanouchi, T. *Tables of Molecular Vibrational Frequencies*, NSRDS NBS: p 39.
- (43) Yang, K.; Zheng, J.; Zhao, Y.; Truhlar, D. Tests of the RPBE, revPBE, τ -HCTHhyb, ω B97X-D, and MOHLYP density functional approximations and 29 others against representative databases for diverse bond energies and barrier heights in catalysis. *J. Chem. Phys.* **2010**, *132*, 164117–10.
- (44) Frisch, M. J.; Trucks, G. W.; Schlegel, H. B.; Scuseria, G. E.; Robb, M. A.; Cheeseman, J. R.; Scalmani, G.; Barone, V.; Mennucci, B.; Petersson, G. A.; Caricato, M. *Gaussian 09*; Gaussian Inc.: Wallingford, CT, 2009.
- (45) Ernzerhof, M.; Scuseria, G. E. Assessment of the Perdew–Burke–Ernzerhof exchange-correlation functional. *J. Chem. Phys.* **1999**, *110*, 5029–5036.
- (46) Sayle, T. X. T.; Parker, S. C.; Catlow, C. R. A. The role of oxygen vacancies on ceria surfaces in the oxidation of carbon monoxide. *Surf. Sci.* **1994**, *316*, 329–336.
- (47) French, S. A.; Sokol, A. A.; Bromley, S. T.; Catlow, C. R. A.; Sherwood, P. Identification and characterization of active sites and their catalytic processes—the Cu/ZnO methanol catalyst. *Top. Catal.* **2003**, *24*, 161–172.
- (48) Dutta, G.; Sokol, A. A.; Catlow, C. R. A.; Keal, T. W.; Sherwood, P. Activation of Carbon Dioxide over Zinc Oxide by Localised Electrons. *ChemPhysChem* **2012**, *13*, 3453–3456.
- (49) Marcus, P. M.; Qian, X.; Hubner, W. Surface stress and relaxation in metals. *J. Phys.: Condens. Matter* **2000**, *12*, 5541.
- (50) Duffy, D. M.; Hoare, J. P.; Tasker, P. W. *J. Phys. C: Solid State Phys.* **1984**, *17*, L195–L199.
- (51) Younglove, B. A. Thermophysical Properties of Fluids. *J. Phys. Chem. Ref. Data* **1982**, *11*, Suppl. 1.
- (52) Keer, H. V. *Principles of Solid State*; Wiley: New York, 1993.
- (53) Hong, J.; Hu, Z.; Probert, M.; Li, K.; Lv, D.; Yang, X.; Gu, L.; Mao, N.; Feng, Q.; Xie, L.; Zhang, J.; Wu, D.; Zhang, Z.; Jin, C.; Ji, W.; Zhang, X.; Yuan, J.; Zhang, Z. Exploring atomic defects in

molybdenum disulphide monolayers. *Nat. Commun.* **2015**, *6*, 629310.1038/ncomms7293.

(54) Logadottir, A.; Nørskov, J. K. The effect of strain for N₂ dissociation on Fe surfaces. *Surf. Sci.* **2001**, *489*, 135–143.

(55) Shetty, S.; Jansen, A. P. J.; van Santen, R. A. Direct versus hydrogen-assisted CO dissociation. *J. Am. Chem. Soc.* **2009**, *131*, 12874–12875.

(56) Hibbitts, D.; Iglesia, E. Prevalence of Biomolecular Routes in the Activation of Diatomic Molecules with Strong Chemical Bonds (O₂, NO, CO, N₂) on Catalytic Surfaces. *Acc. Chem. Res.* **2015**, *48*, 1254–1262.